THE ASTROPHYSICAL JOURNAL, 554:1035–1043, 2001 June 20

CHANDRA OBSERVATIONS OF "THE ANTENNAE" GALAXIES (NGC 4038/9)

G. FABBIANO, A. ZEZAS, AND S. S. MURRAY
Harvard-Smithsonian Center for Astrophysics, 60 Garden Street, Cambridge, MA 02138
Received 2000 October 16; accepted 2001 February 21

ABSTRACT

We report the results of a deep *Chandra* ACIS pointing at the merging system NGC 4038/9. We detect an extraordinarily luminous population of X-ray sources, with luminosity well above that of XRBs in M31 and the Milky Way. If these sources are unbeamed XRBs, our observations may point to them being 10–(a few)100 $M_\odot$ black hole counterparts. We detect an X-ray bright hot ISM, with features including bright superbubbles associated with the actively star-forming knots, regions where hot and warm (Hα) ISM intermingle, and a large-scale outflow.

Subject headings: galaxies: individual (NGC 4038/9) — galaxies: interactions — galaxies: peculiar — X-rays: galaxies

On-line material: color figure

1. INTRODUCTION

NGC 4038/9 (modeled by Toomre & Toomre 1972 and Barnes 1988) are the nearest pair of colliding galaxies involved in a major merger ($D = 29$ Mpc, for $H_0 = 50$). Hence, this system provides a unique opportunity for getting the most detailed look possible at the consequences of a galaxy merger as evidenced by induced star formation and the conditions in the ISM.

Each of the two colliding disks shows rings of giant H II regions and bright stellar knots with luminosities up to $M_V \sim -16$ (Rubin et al. 1970), which are resolved with the *Hubble Space Telescope* into typically about a dozen young star clusters (Whitmore & Schweizer 1995). These knots coincide with the peaks of Hα, 2.2 μm, and 6 cm radio-continuum emission (Amram et al. 1992; Stanford et al. 1990; Hummel & van der Hulst 1986), indicating an intensity of star formation exceeding that observed in 30 Doradus. CO aperture synthesis maps reveal major concentrations of molecular gas, including $\sim 2.7 \times 10^9\ M_\odot$ in the region where the two disks overlap (Stanford et al. 1990; Wilson et al. 2000). A recent K-band study derives ages for the star clusters ranging from 4 to 13 Myr, and measures high values of extinction ($A_V \sim 0.7$–4.3 mag; Mengel et al. 2000).

X-ray emission from the Antennae was first observed with the *Einstein* IPC (Fabbiano, Feigelson, & Zamorani 1982; Fabbiano & Trinchieri 1983), with a luminosity of $L_X \sim 1 \times 10^{41}$ ergs s^{-1}, larger than the average X-ray luminosity of normal spiral galaxies (e.g., Fabbiano 1989 and references therein). More recently the Antennae have been studied with the *ROSAT* PSPC (Read, Ponman, & Wolstencroft 1995), *ROSAT* HRI (Fabbiano, Schweizer, & Mackie 1997), and *ASCA* (Sansom et al. 1996). These instruments reveal different emission components, including soft gaseous emission, which Read et al. suggested may be connected with a bipolar outflow, and harder emission. The 5″ resolution *ROSAT* HRI image reveals very complex and intricate X-ray emission, clearly dominated by components associated with the recent star formation activity, and suggests both an exceptional population of superluminous pointlike sources (three were detected with $L_X \sim 6 \times 10^{39} - 1 \times 10^{40}$ ergs s^{-1}), and a possibly extended and filamentary hot ISM (Fabbiano et al. 1997).

In this paper we present the first results of a deep *Chandra* ACIS (Garmire 1997; Weisskopf et al. 2000) observation of the Antennae. The spatial resolution of *Chandra* is 10 times superior to that of the *ROSAT* HRI, allowing us to resolve the emission on physical sizes of ~ 70 pc, versus the ~ 700 pc resolution possible with the *ROSAT* HRI. With this resolution we can easily detect individual X-ray sources and image in detail the spatial properties of more extended emission regions. At the same time, ACIS allows us to study the X-ray spectral properties of these sources and emission regions, providing additional important constraints on their nature, something that was not possible with the HRI.

Here we summarize the overall results, as they pertain to the general morphology of the X-ray emission and to the detection of the different compact and gaseous X-ray emitting components. A detailed analysis of the point source component of NGC 4038/9 will be presented in Zezas et al. (2001, in preparation, hereafter Paper II). A detailed spectral analysis of the diffuse component and a multi-wavelength comparison of the ISM will be presented in Fabbiano et al. (2001, in preparation, hereafter Paper III).

2. OBSERVATIONS AND DATA ANALYSIS

Chandra was pointed to NGC 4038/9 on 1999 December 1 for 72.5 ks with the back-illuminated ACIS-S3 CCD chip at the focus (Observation ID: 315). ACIS was at a temperature of -110 C during these observations. The satellite telemetry was processed at the *Chandra* X-ray Center (CXC) with the Standard Data Processing (SDP) system, to correct for the motion of the satellite and to apply instrument calibration. The data used for this work were processed in custom mode with the version R4CU5UPD6.5 of the SDP, to take advantage of improvements in processing software and calibration, in advance of data reprocessing. Verification of the data products showed no anomalies. The data products were then analyzed with the CXC CIAO software. CIAO Data Model tools were used for data manipulation, such as screening out bad pixels, and producing images in given energy bands. The 2000 April release of the ACIS CCD calibration files (FEF) was used for the analysis.

In preparation for further analysis the data were screened to exclude the two "hot" columns present in ACIS-S3 at chip-x columns 512 and 513 (at the b and c node

boundaries). Besides causing stripes in the image, these hot columns contaminate the source spectrum at the low energies (near 0.2 keV), as can be seen from Figure 1, where we show the integrated source count spectral distribution before and after the screening.

No screening to remove high background data was necessary: the light curve extracted from an area of 7 arcmin^2 showed a constant count rate of 0.456 ± 0.004 counts s^{-1}, consistent with a low-level background radiation.

After completion of this work, the reprocessed *Chandra* data products became available. While these data are generally consistent with those used in this paper, and therefore our results and conclusions stand, the aspect calibration was improved giving an improved absolute source position with 1 σ error of 0.″6. The R4CU5UPD6.5 data instead have an absolute position error of $\sim$1.″8, which we have estimated by using stars in the field detected in X-rays. The revised absolute positions are consistent with our astrometry. We have used the latest and best *Chandra* positional information for our comparison with other positional information (optical, CO, *ROSAT* HRI, Hα) later on in this paper.

2.1. *Characteristics of the Overall X-Ray Emission*

Figure 2 shows the full-band (0.1–10 keV) ACIS-S3 field including the Antennae galaxies. The data here are shown without any processing, beside that described above. It is clear that the emission is complex, consisting of diffuse emission regions of varying intensity and sizes, and of a number of bright pointlike sources. On Figure 2 are displayed a number of regions. The polygon, surrounding the emission area associated with the Antennae galaxies, was chosen to be inclusive of the area covered by the optical images of these galaxies; this region was used to extract the total source counts and spectral counts as discussed later in this paper. The circles surrounding this polygon are the background extraction areas for these estimates. Pointlike sources were excluded from the background areas (*dashed circles*).

Figure 3*a* displays an adaptively smoothed image of the full-band ACIS image of NGC 4038/9, generated with the CIAO task "csmooth," which adjusts the smoothing kernel in order to preserve a constant S/N across the image. Each pixel in the input image is smoothed on its "natural" scale, in the sense that the smoothing scale is increased until the total number of counts under the kernel exceeds a value that is determined from a preset significance and the expected number of background counts in the kernel area. In our case, csmooth was set to perform the background calculation locally. The smoothing function we used is a variable-width two-dimensional Gaussian and the S/N was set to range between 3 and 5 over the image. In Figure 3*b* we also show an outline of the optical image of the interacting galaxy disks (*white contours*), the positions of the two nuclei ("X"), the positions of peaks of the CO distribution, indicating the areas of highest obscuration (*crosses*; Stanford et al. 1990), and circles representing the source extraction areas of the three possibly pointlike sources detected with the *ROSAT* HRI (X-3, X-11, X-12; Fabbiano, Schweizer, & Mackie 1997). Comparison with the *ROSAT* PSPC, *ASCA*, and *Einstein* images is meaningless given the significantly lower resolution of these telescopes (see Fabbiano et al. 1997 for a comparison between *ROSAT* HRI and earlier, lower angular resolution data). In general, however, our results confirm early findings pointing to a complex X-ray emission field. The X-ray image shows clearly a number of bright pointlike sources, extended emission associated with the numerous star formation regions in the two disks and with the nuclear regions, and lower surface brightness emission associated with the entire stellar system, and possibly extending beyond it.

Figure 4 is a true X-ray color image, where red corresponds to 0.1–2.0 keV, green to 2.0–5.0 keV, and blue to 5.0–10.0 keV. Images in each of the three bands were adaptively smoothed, as described above. To produce this figure, the three images were then combined using the CIAO tool "dmimg2jpg," which makes a color JPEG image (or EPS) from three image files. This color image shows that the

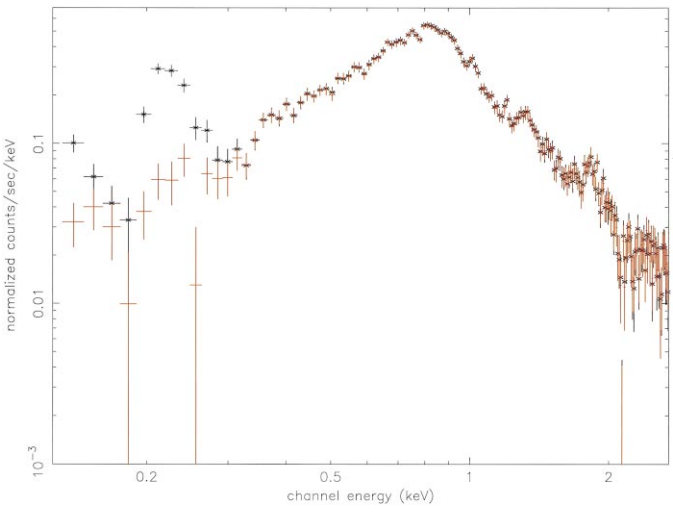

FIG. 1.—Energy distribution of the integrated source counts (from the polygon in Fig. 2, after background subtraction) before (*black* "x") and after (*red*) removal of the hot columns (see text).

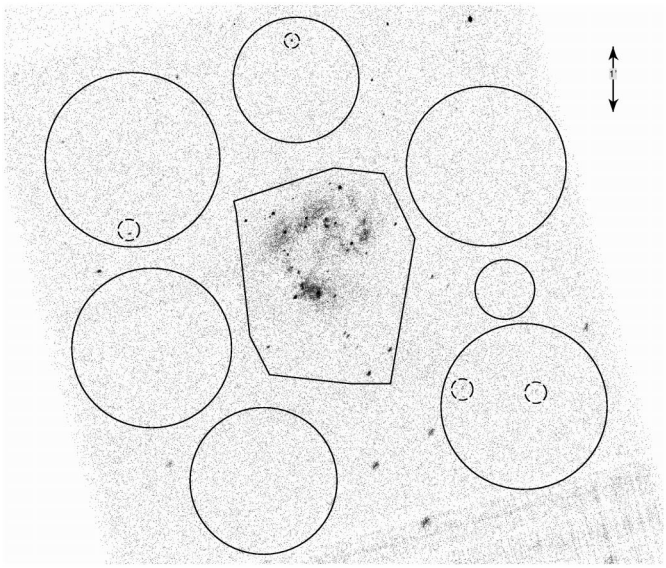

FIG. 2.—Screened but otherwise unprocessed full energy range (0.1–10.0 keV) back-illuminated ACIS-S3 image. Most of the 8′ × 8′ S3 CCD field is displayed. The polygon represents the source area, and the large circles the background areas (see text). The dashed circles are regions excluded from the background calculation. [*See the electronic edition of the Journal for a color version of this figure.*]

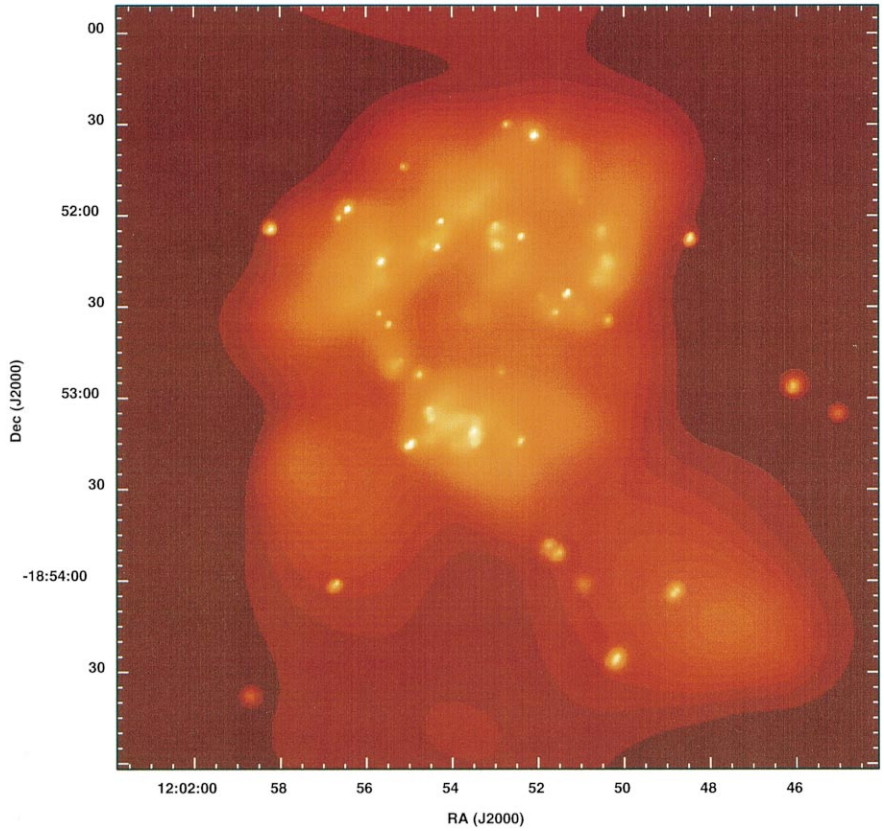

FIG. 3*a*

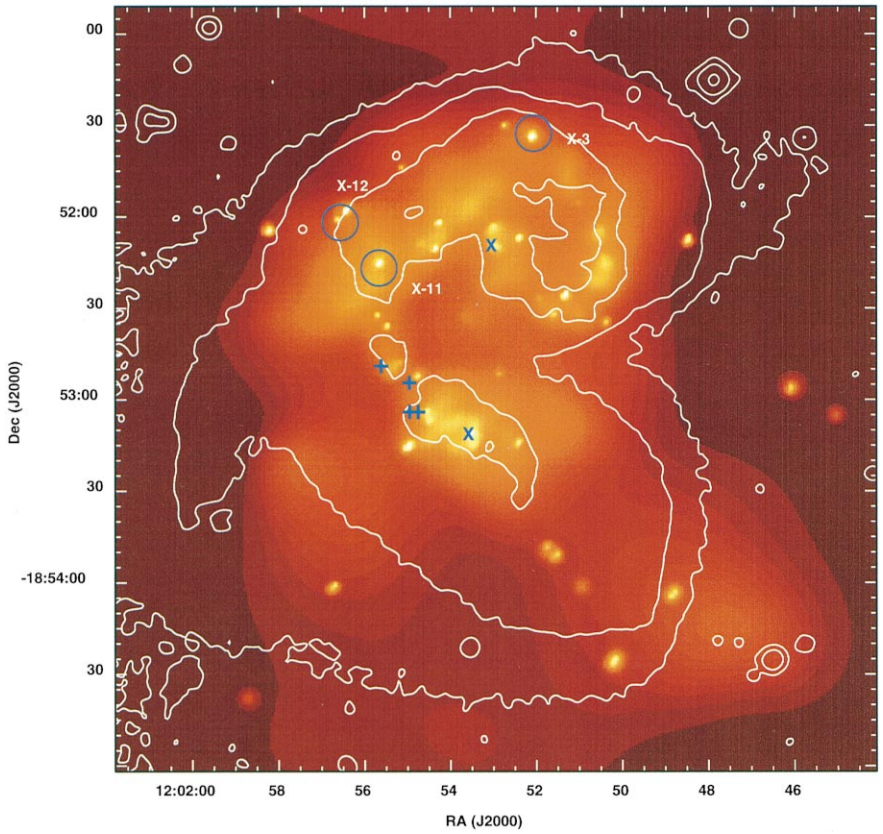

FIG. 3*b*

FIG. 3.—(*a*) Adaptively smoothed broadband (0.1–10 keV) image of the Antennae galaxies. (*b*) Same as the preceding figure, but with overlays representing the optical contours from the POSS digital survey (*white*), blue crosses representing the CO emission peaks (Stanford et al. 1990), blue "X" marking the positions of the two nuclei, and blue circles identifying three pointlike sources detected with the *ROSAT* HRI (Fabbiano et al. 1997).

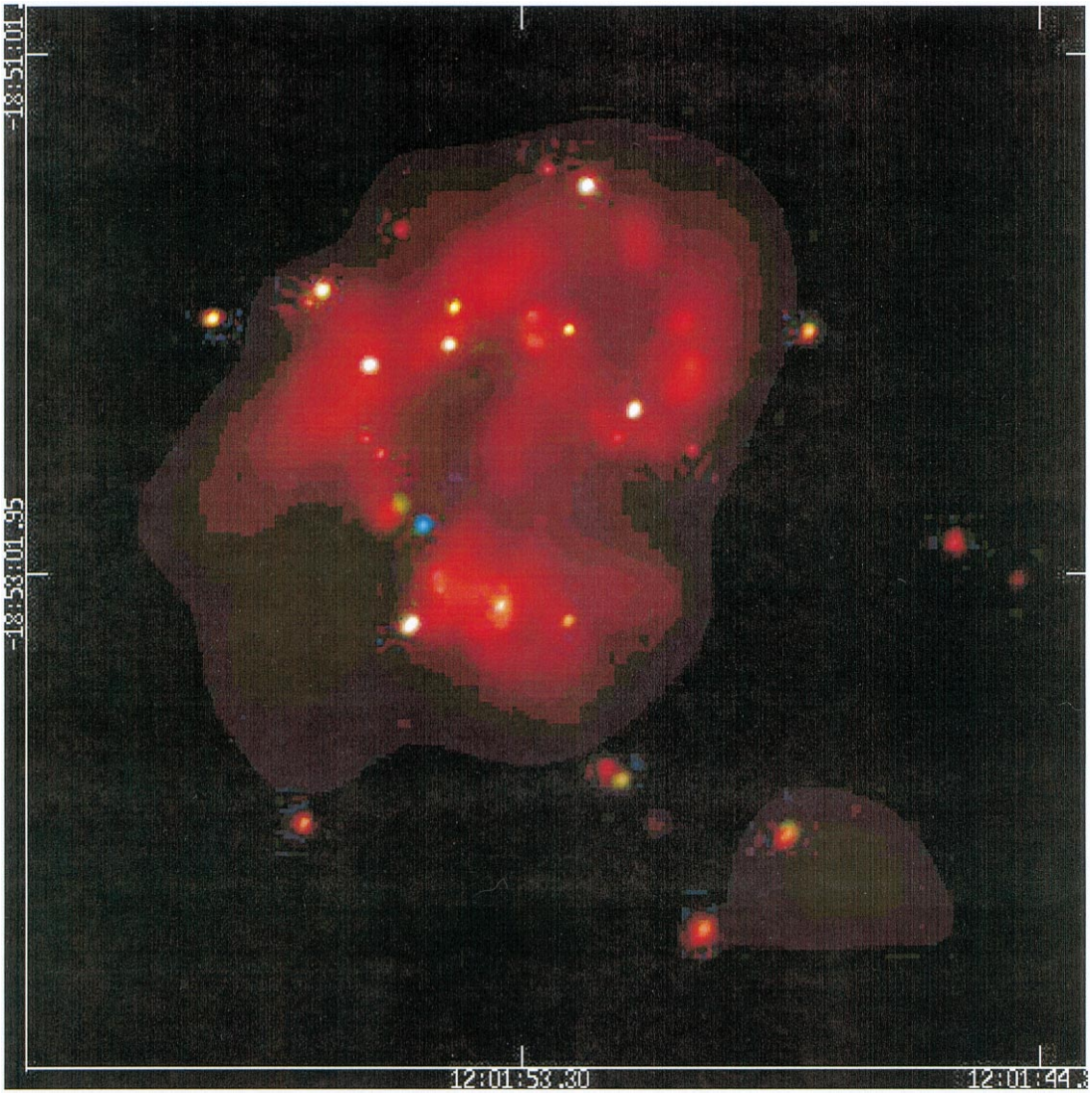

FIG. 4.—Adaptively smoothed X-ray "true" color image. *Red*, 1.0–2.0 keV; *green*, 2.0–5.0 keV; *blue*, 5.0–10.0 keV

bright pointlike sources have harder spectra than the diffuse emission: they appear white, implying that they emit in all three energy bands, with the exception of a "blue" heavily absorbed source, in the area of most intense CO emission (Stanford et al. 1990; see Fig. 3*b*, also note some "green" emission nearby, also indicative of X-ray absorption). The diffuse emission instead is softer (red in the image), but it also shows some harder areas, for example in the vicinity of the nucleus of NGC 4039 (the southern galaxy; see Fig. 3*b* for the position of the nucleus).

Figure 5 shows the spectral distribution of the detected counts from NGC 4038/9 (*black*), the co-added spectrum of detected sources (*blue*), which is dominated by the luminous pointlike sources, but includes a few faint, possibly extended sources (see below), a representative bright pointlike source spectrum (*green*), and the spectrum of the diffuse emission (*red*), obtained by excluding the contributions of pointlike and small-scale extended sources from the image. The area used for the extraction of the integrated galaxian emission is shown by the polygon in Figure 6 (also Fig. 2). The background counts were derived from the circular regions marked in Figure 2. The detected source regions that were subtracted from the overall source area are shown by circles and ellipses in Figure 6. The four largest ellipses (*dashed*) indicate the presence of diffuse and possibly complex emission and were excluded from the spectral count extraction.

A detailed discussion of source detection and point-source spectral analysis is given in Paper II. We find that there is a range of source spectra, but the most luminous ones tend to be quite hard. This is consistent with what is shown in Figure 5, where the point-source subtraction results in the lack of emission from the higher energy channels. The spectrum of the diffuse emission has features pointing to the optically thin thermal emission of a hot plasma (Fe-L complex; Mg Kα; Si Kα). Note that in Figure 5 the integrated galaxian spectrum becomes noise-dominated around 5 keV, while the co-added and individual bright source spectra are still significant at higher energies. This is because the general integrated spectrum is derived from a large area that becomes background dominated at the higher energies. The individual detected-source counts instead were extracted from the small source areas of Figure 6.

2.2. *Pointlike Sources*

We detect 48 sources at the 3 σ level with CIAO's "wavdetect," using scales from 1 to 16 pixels (0.″5–8″); 43 are detected in the 0.1–10.0 keV band, two only in the 2.0–

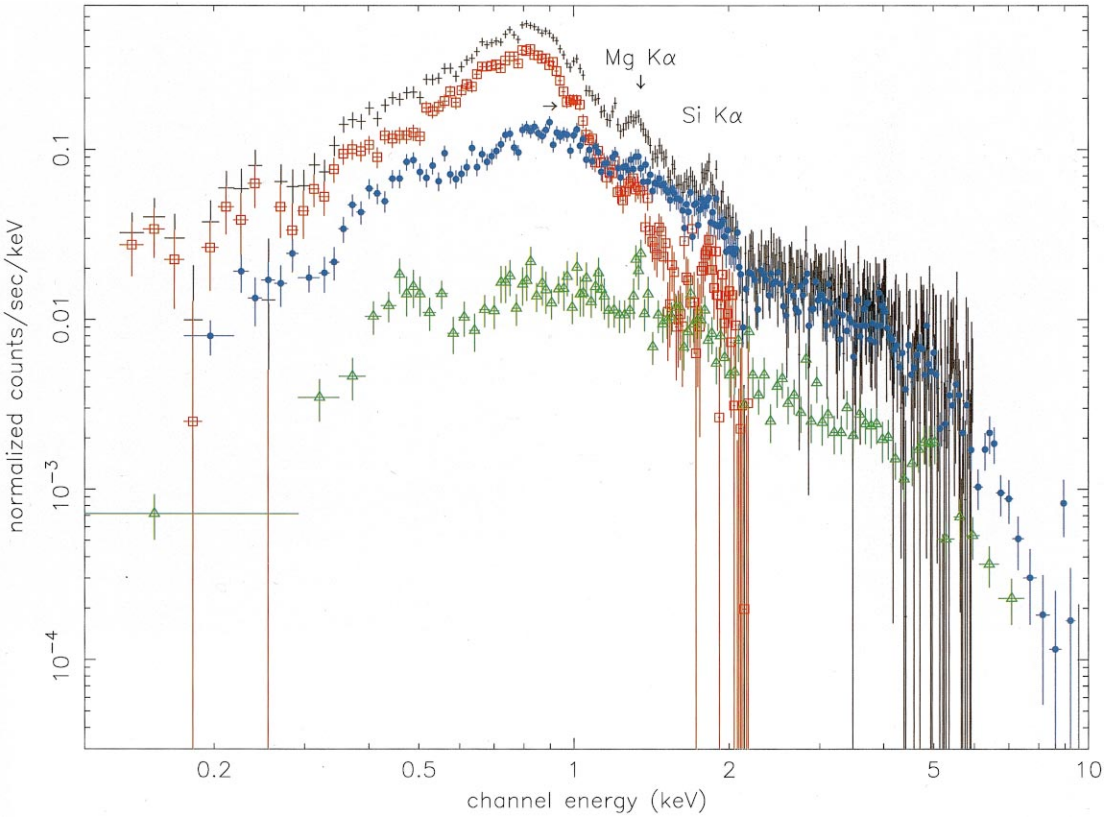

FIG. 5.—Observed ACIS-S3 spectral count distribution of the entire emission from the Antennae (*upper points; black*), the co-added emission of detected sources (*blue filled circles*), and the diffuse emission, obtained by excluding all the detected sources from the image (*red squares*). The green triangles display the spectrum of an individual bright pointlike source. Emission lines of the hot interstellar plasma (Mg Kα, Si Kα) are identified. The Fe L complex is the broad peak just below 1 keV.

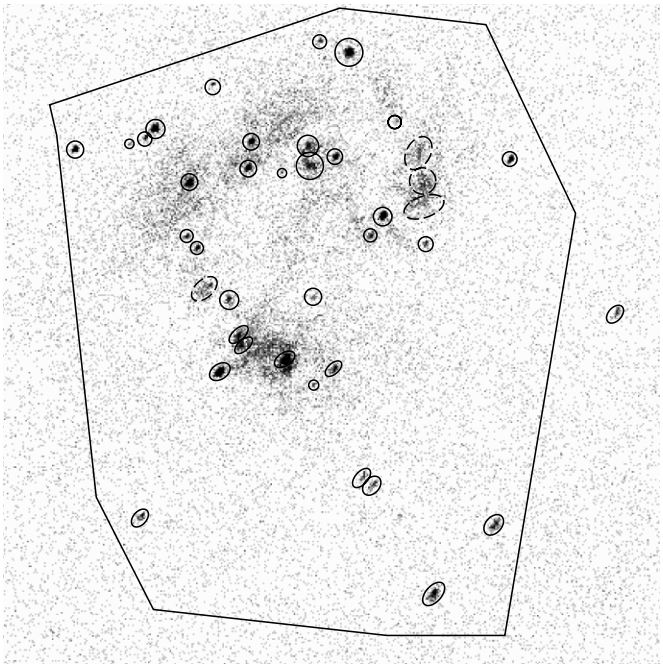

FIG. 6.—Unsmoothed image of the Antennae. The polygon is the same as in Fig. 2. The circles and ellipses identify sources (or emission complexes) detected with wavdetect. Dashed ellipses are complex and/or diffuse emission regions.

4.0 keV, and three only in the 0.1–2.0 keV band; 10 of these 48 sources can be identified with small-size features of the extended emission regions, while the rest appear pointlike. The latter include all the bright sources visible in the images we have shown earlier in this paper. Pointlike detections range from 10 to 2063 counts per source and account for 35.6% of the entire NGC 4038/9 counts in the 0.1–10.0 keV band. In the "soft" (0.1–2.0 keV) band point sources produce 31.5% of the total emission, whereas they dominate the X-ray emission in the "hard" band (2.0–10.0 keV), accounting for 81.4% of the total. At a distance of 29 Mpc, the "pointlike" individual sources have an intrinsic luminosity ranging from 1.3×10^{38} ergs s^{-1} to 2.0×10^{40} ergs s^{-1}, where we have used a 5 keV bremsstrahlung model with galactic neutral hydrogen column density along the line of sight ($N_H = 3.4 \times 10^{20}$ cm^{-2}) for all the sources detected in the 0.1–10.0 keV band, and spectra suggested by the spectral analysis (Paper II) for the soft and mid-range detected sources. Since these sources are likely to be absorbed because of the dusty environment in the host galaxies (most remarkably, the "blue" source in Fig. 4), or may have some intrinsic absorption, these luminosities are likely to be lower limits to the real emitted source luminosities. Full details of the source detection analysis and results are given in Paper II.

Three pointlike sources were reported by Fabbiano et al. (1997) from the analysis of the *ROSAT* HRI image. Of these

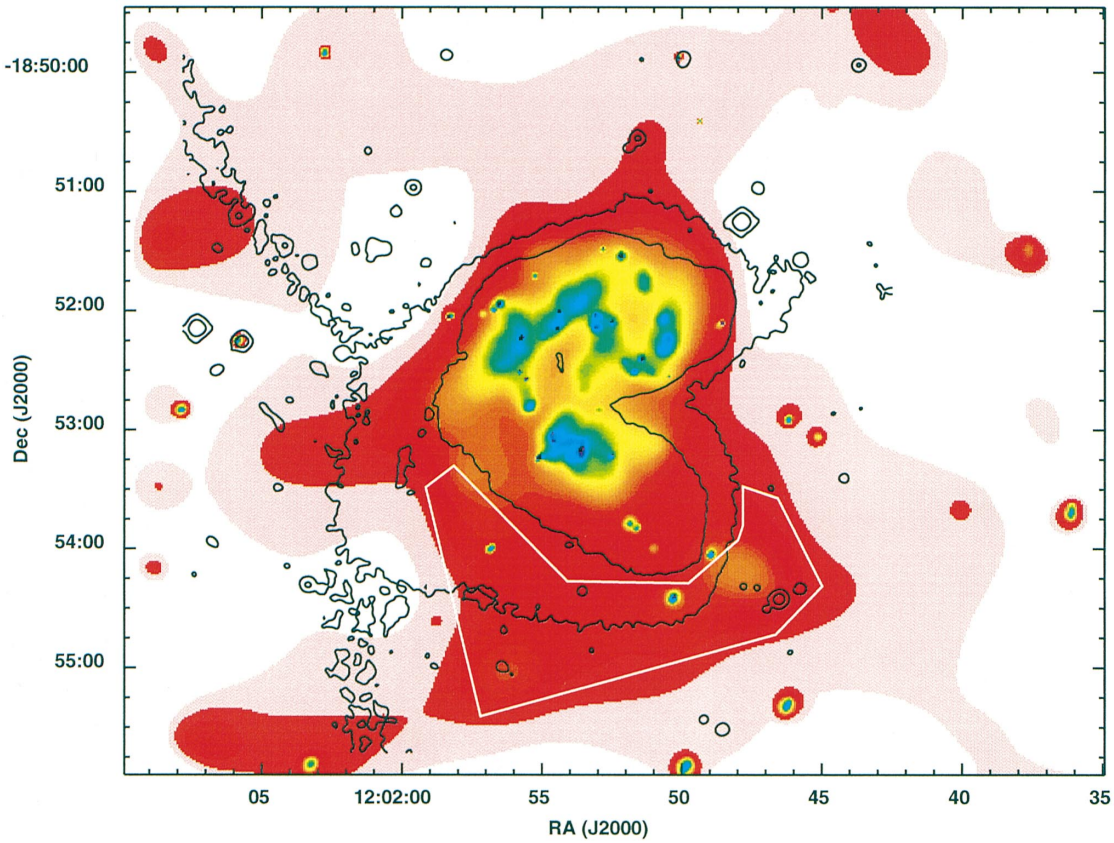

FIG. 7.—Wide-field adaptively smoothed image, with data binned in 1″ pixels. The color scale of the X-ray image was chosen to highlight the low surface brightness diffuse emission (*in red*). Peaks of the surface brightness distribution are displayed in blue. Optical contours are displayed on this image, which shows low-surface brightness X-ray emission extending to the south of the optical image. The polygon to the south of the main body of the optical emission was used to estimate the X-ray luminosity of this low-surface brightness X-ray component.

(see Fig. 3*b*), source X-3 is coincident with a *Chandra* source; X-11 includes both a bright *Chandra* source and diffuse emission; X-12 includes two *Chandra* sources. Note, however, that the *ROSAT* positions may be affected by a few arcseconds aspect uncertainties, and also by the fact that the *ROSAT* HRI sources were detected with 20–27 counts, which also include sizeable contributions from whatever else is in the source region. Under these circumstances the source centroid would not be very accurate, because of detection statistics, and would also be biased by the surrounding emission.

The great majority of the detected pointlike sources are associated with NGC 4038/9. Using the *Chandra* Deep Field (Giacconi et al. 2000) estimates, the number of background sources expected from a comparable area ($\sim$5.9 square arcminutes) is 1.7 at our soft band ($<$2 keV) flux threshold of 4×10^{-16} ergs cm^{-2} s^{-1}. In this band we detect 34 pointlike sources. At our hard band ($>$2 keV) flux threshold of 2.8×10^{-15} ergs cm^{-2} s^{-1}, we expect 1.4 background sources, and we detect 20 sources in the Antennae. Given the presence of extended emission local to NGC 4038/9, we estimate that our source detection completeness limit is a few 10^{38} ergs s^{-1}.

2.3. *Extended X-Ray Emitting Regions*

The *Chandra* images show extended emission features with sizes ranging from a few arcseconds (few hundred parsecs) to scales of the order of the entire galaxian system or larger. A complete study of the spatial and spectral characteristics of this emission requires a better calibration of the low-energy response function of *Chandra* ACIS than was available at the time of the present work, and so will be deferred to Paper III. We can still, however, summarize the principal characteristics of this emission.

As mentioned in § 2.2, 10 of the relatively small-size sources detected in the Antennae are not pointlike. Some of these sources are easily identifiable as peaks of the diffuse emission component within the Antennae "heads." These extended bright emission regions have luminosities in the 10^{39-40} ergs s^{-1} range, assuming a thermal Raymond-Smith spectrum of $kT = 0.8$ keV and galactic line of sight $N_{\rm H}$.

The two nuclear regions are among the extended sources. At least in the case of the southern nucleus, the emission temperature may be higher than that of the emission associated with star forming knots in the arms (see Fig. 4, the X-ray color map, that shows some "white" in the southern nucleus area). Assuming a thermal spectrum with $kT = 5$ keV and line of sight $N_{\rm H}$, we obtain luminosities of 1.3×10^{40} ergs s^{-1} and 1.5×10^{40} ergs s^{-1} for the northern and southern nuclear regions, respectively. The nuclear regions may be 40% fainter if the emission is significantly softer ($kT \sim 0.8$ keV), as it is more likely to be the case for the northern nucleus.

We examined the ACIS image in the soft band (0.1–2.0 keV) for evidence of the large-scale galaxian outflow (or halo) suggested by Read, Ponman, & Wolstencroft (1995) on the basis of the low angular resolution ($\sim$25″) *ROSAT*

PSPC image. While our results are very preliminary and need to be confirmed with a proper spatial/spectral analysis of the extended soft emission (Paper III), we note some low surface brightness, but significant, emission extending mostly to the south of the optical body in the ACIS image. This is shown in Figure 7, where we display the results of an adaptive smoothing of a wide field section of the ACIS-S3 chip, with the data previously binned by a factor of 2, resulting in 1″ image pixels. Analysis of the raw data shows that the X-ray surface brightness excesses seen in these regions range from 40% to 10% over the lower surface brightness (background) areas in the image. These excesses cannot be explained with instrumental nonuniformities, because the maximum *expected* excursions from similar areas are of 5% at the most, based on the instrumental Quantum Efficiency Uniformity map and mirror vignetting. In the south, for the same spectral assumptions as those used for the soft diffuse emission within the Antennae, we estimate a luminosity for this very extended low-surface-brightness component of $\sim(7.5 \pm 0.2) \times 10^{39}$ ergs s^{-1}, assuming a Raymond-Smith spectrum with $kT = 0.8$ keV and $N_{\rm H} = 3.4 \times 10^{20}$ cm^{-2}.

2.4. *Luminosities of the Emission Components*

With the same spectral assumptions as above for the different galaxian components, the total (0.1–10) keV luminosity of NGC 4038/9 is 2.3×10^{41} ergs s^{-1}. The total point-source contribution is 1.1×10^{41} ergs s^{-1}, roughly half of the luminosity, and the thermal extended components (including the nuclear regions) account for the remaining 1.2×10^{41} ergs s^{-1}. Considering the amount of guesswork involved in earlier estimates, which did not have the benefit of *Chandra*'s resolution, these estimates are in general agreement with those of Fabbiano et al. (1997).

3. DISCUSSION

The *Chandra* observation of the Antennae demonstrates how exceptional the X-ray emission of merging galaxies may be, in comparison with that of individual relatively undisturbed spiral systems (e.g., Fabbiano 1989, 1995). In the Antennae we detect a population of superluminous discrete X-ray sources, a very luminous hot ISM, and two bright complex starburst nuclear regions. While these components were suggested by the *ROSAT* HRI observations (Fabbiano et al. 1997), it is only with the combined subarcsecond spatial and spectral resolution of *Chandra* ACIS that we can firmly establish their presence and properties.

3.1. *A Population of Massive Black Hole Binaries?*

Figure 8 shows the luminosity distribution of "pointlike" sources detected in the ACIS observation, compared with the upper end of the luminosity distribution of X-ray sources (most likely accretion binary systems, XRBs) in M31 (from *Einstein*, Trinchieri & Fabbiano 1990; note that given the distances of the two systems, the physical resolution of the *Chandra* observation of NGC 4038/9 is within a factor of 2 that of the *Einstein* HRI of M31). In the case of NGC 4038/9 we plot two histograms, corresponding to two different choices of H_0: the filled one for $H_0 = 50$, and the dashed one for $H_0 = 75$. The M31 and the NGC 4038/9 histograms have been arbitrarily plotted in different scales, for ease of display. The point of this comparison is

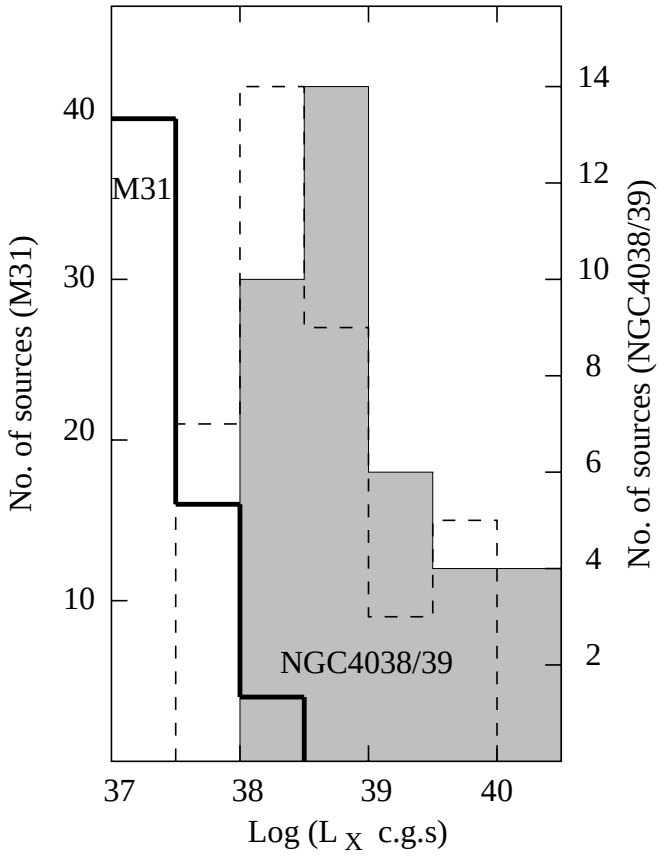

FIG. 8.—Histogram of the luminosity distribution in NGC 4038/9 (*filled*, $H_0 = 50$; *dashed*, $H_0 = 75$), compared with that of M31.

not to compare the total number of fainter sources in the two systems, since the different incompleteness biases prevent it. However, in both cases, there are no such effects at luminosities higher than a few 10^{38} ergs s^{-1}.

In M31, and the Milky Way (e.g., Watson 1990), XRBs have luminosities consistent with the Eddington limit of ~ 1 solar mass accreting object ($\sim 1.3 \times 10^{38}$ ergs s^{-1}). In the Antennae instead we find 14–8 (depending on H_0) sources with luminosities of 1×10^{39} ergs s^{-1} or above, reaching as high as $\sim 10^{40}$ ergs s^{-1}. One of these sources (X-3) was detected, as possibly variable, with *ROSAT* (Fabbiano et al. 1997).

Superluminous "Super-Eddington" sources were detected in some nearby galaxies prior to *Chandra* (e.g., Fabbiano 1995), and for some of them at least there is spectral evidence of accretion disks from *ASCA*, pointing to a black-hole binary counterpart (Makishima et al. 2000). These sources tended to be associated with star-forming regions, but they were rare, and the lack of angular resolution allowed the possibility of bright clumps of X-ray sources in most cases.

What we see now is a population of these sources in a single galaxian system. As discussed by Fabbiano et al. (1997), their large X-ray luminosities exclude that we are seeing the integrated stellar coronal emission of the star-forming knots. These luminous sources have hard spectra, reminiscent of galactic XRBs, very unlike the thermal spectra of the more diffuse emission regions (Figs. 4 and 5; Paper II). Given their luminosities, that are comparable

with, or exceed, the total integrated luminosity of M31, it is unlikely that they could be clumps of "normal" XRBs. We would need a few tens to a hundred neutron star binaries (the entire X-ray emitting population of a normal spiral galaxy), clustered in areas with 100 pc typical sizes.

If these sources are single XRBs, their luminosities suggest 10–100 (or larger) $M_\odot$ black-hole counterparts, unless they are all beamed. The detection of soft excesses in their spectra (as in the sources studied by Makishima et al. 2000) would favor the black-hole hypothesis. This will have to await the soft-band calibration of ACIS. It is possible that at least some of these superluminous sources may be very young Supernovae (e.g., Schlegel 1995). Future monitoring of the Antennae is needed to verify this possibility. Any detection of variability, other than secular fading, would point to XRBs, e.g., as in the galaxy Holmberg II, where the compact object is estimated to be a $\sim 200\ M_\odot$ black-hole candidate (Zezas, Georgantopoulos, & Ward 1999), or as recently reported for M81 X-9 (La Parola et al. 2001). Similarly luminous sources, albeit in smaller number, are detected in M82 with *Chandra*. In M82, the detection of variability (Kaaret et al. 2000; Zezas et al. 2000; Matsumoto et al. 2001) demonstrates their XRB nature.

The presence of a copious number of these superluminous sources in galaxies undergoing violent starbursts, such as NGC 4038/9 and M82, and their absence from more settled galaxies, with an older stellar population, suggests that they are short-lived objects. This may be consistent with a fast-evolving massive black hole binary hypothesis. This scenario has an interesting corollary: if what we see in the Antennae today was the norm at the epoch of galaxy formation, then any spiral galaxy, such as our own Milky Way, may have an invisible population of massive black holes, the remnants of primordial massive stars and of spent superluminous XRBs. A number of these systems may have sunk to the nucleus (Tremaine, Ostriker, & Spitzer 1975) and contributed to the formation of massive nuclear black holes.

However, it is also possible that the compact counterparts of these superluminous sources are more modest black holes, with masses in the range of galactic black hole binaries, if mild beaming is allowed. These possibilities are discussed in King et al. (2001).

Superluminous hard sources in distant young galaxies may also be an alternate explanation for the hard deep survey sources identified with galaxies with no sign of activity and explained with obscured active galactic nuclei (Hasinger 1999). In the Antennae, the integrated luminosity of superluminous sources is $\sim 10^{41}$ ergs s^{-1}. Their contribution to large galaxies in formation may be substantial.

3.2. *The Hot ISM*

The *Chandra* ACIS data reveal a spectacular and varied hot ISM that had been only glimpsed at with previous *ASCA* and *ROSAT* observations (Sansom et al. 1996; Read et al. 1995; Fabbiano et al. 1997). While a detailed analysis of this multiphase ISM will be reported in a follow-up paper, here we note that a comparison of the *Chandra* image with the archival *HST* WFPC-2 Hα-filter image of NGC 4038/9 (Fig. 9) suggests an interesting and intricate picture of the multiphase ISM. The X-ray data in Figure 9 were smoothed with a 2 pixel (1″) Gaussian, to retain the small-scale details. The X-ray contours are overlaid onto the Hα image. We used the reprocessed *Chandra* data with the latest improved absolute position for this overlay (see § 2), which agrees with our astrometry based on field stars detected in X-rays. However, we have no way to check the astrometry of the Hα image with the available data.

Although there is a general similarity between the distributions of hot and cooler ISM, the two are not identical. We find regions where Hα and X-ray emission are both enhanced, e.g., regions E and F, where the X-ray and Hα peaks pretty much coincide, suggesting that the Hα and X-ray emitting gases are finely intermingled, but still retain their different temperatures. A similar situation is observed in the nuclear outflow of M82 (e.g., Watson, Stanger, & Griffiths 1984). But we also find Hα cavities that correspond to peaks of the X-ray emission, suggesting a number of "superbubbles," where X-ray hot gas appears to fill a hole in the Hα emitting-gas distribution (regions A, B, possibly

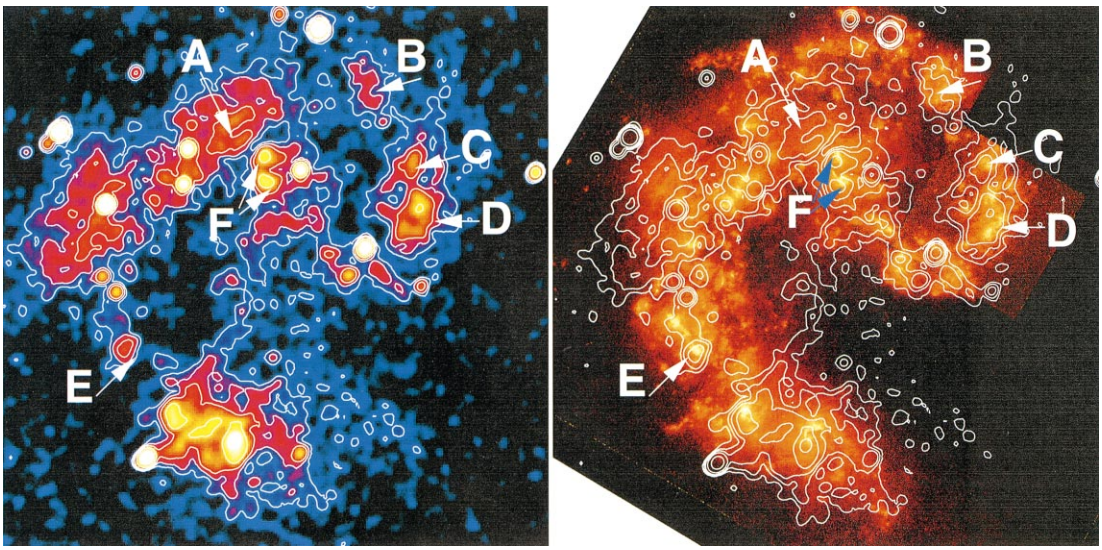

FIG. 9.—*Left*: X-ray image smoothed with a 1″ Gaussian together with isointensity contours. *Right*: X-ray contours overlaid on the *HST* WFPC-2 Hα filter archival image of the Antennae.

C, D in Fig. 9). Typical diameters and luminosities of these Hα-bound hot regions are $\sim$1.5 kpc and $\sim 10^{39-40}$ ergs s^{-1}. These superbubbles are extraordinary, if we compare them with already studied superbubbles in the more nearby universe. Their X-ray luminosities are a factor of 10–100 larger than those of the gaseous emission of the 30 Doradus nebula in the LMC (Wang & Helfand 1991), and of the superbubbles in M101, that have typical luminosities of $\sim 1 \times 10^{38}$ ergs s^{-1} (Williams & Chu 1995). Assuming temperatures of $\sim 5 \times 10^6$ K and spherical emission volumes of 1.5 kpc diameter, we derive typical masses of hot gas in these regions of $10^{5-6}\ M_\odot$.

The nuclear regions of the two galaxies (see § 2) also appear associated with extended thermal features, as had been suggested by Fabbiano et al. (1997). There are two extended emission regions in the vicinities of the northern nucleus (NGC 4038, see Fig. 3; region F in Fig. 9). The southern nucleus (NGC 4039) is embedded in extended soft emission, but it may contain a harder emission peak (Figs. 3 and 4). Future spectral analysis of the ACIS data may help unravel this source. Note here that there is a slight displacement between some X-ray and Hα features (e.g., regions F in Fig. 9, near the northern nucleus), that may be due at least in part to the compounded uncertainty of the *HST* and *Chandra* astrometry. However, in other cases (e.g., region E), X-ray and Hα peaks pretty much coincide.

Some of the hot X-ray emitting regions in the ISM, and the nuclear regions themselves, may give rise to hot gaseous outflows, like those witnessed in nearby starburst galaxies (e.g., NGC 253 and M82, Fabbiano & Trinchieri 1984; Watson et al. 1984; Fabbiano 1988). The luminosities of the hot gaseous regions in the Antennae, and therefore their thermal energy content, are comparable to or larger than that of the hot gaseous component of the nucleus of NGC 253. Region B in particular shows X-ray emitting plasma surrounded by a shell-like Hα structure at the base of what may be a local outflow, as suggested by the presence of radial tendrils visible in a close inspection of the Hα image. The large-scale N-S extent of the X-ray surface brightness (§ 2.3) suggests the presence of large-scale hot outflowing ISM out to $\sim$8 kpc (in projection) from the galaxy disks.

4. CONCLUSIONS

The *Chandra* ACIS data of the Antennae galaxies offer an excellent example of what high (subarcsecond) spatial resolution, joined with spectral capabilities, can achieve in the X-ray band.

We have discovered a population of extremely luminous pointlike sources, with X-ray luminosities well in excess of the Eddington limit for 1 $M_\odot$ accretor, suggesting a young population of $\sim$10–(a few)100 $M_\odot$ black hole binaries, which are not seen in more evolved stellar populations, such as those of the Milky Way and M31.

We detect soft thermal emission, pointing to a varied hot ISM in these galaxies, presumably powered by the intense star formation. Features of this hot component encompass superbubbles associated with the star-forming knots, circumnuclear features, and an all-pervasive component, extending farther than the stellar bodies of the interacting galaxies and pointing to a galactic scale outflow.

This is our first report of these data. A detailed analysis of the point-source population will be presented in a forthcoming paper (Zezas et al. 2001). A discussion of models of stellar and binary evolution that may explain our data, and of their implications for the massive portion of the IMF of spiral galaxies is the subject of another paper in preparation (King et al. 2001). A detailed analysis of the hot ISM, and comparison with multiwavelength data to obtain a full picture of the multiphase ISM, will be given in Fabbiano et al. (2001).

We thank the CXC DS and SDS teams for their efforts in reducing the data and developing the software used for the reduction (SDP) and analysis (CIAO). We also thank Andrew King, Martin Ward and Martin Elvis for discussions on these results. This work was supported by NASA contract NAS 8-39073 (CXC) and NAS8-38248 (HRC).

REFERENCES

Amram, P., Marcelin, M., Boulesteix, J., & le Coarer, E. 1992, A&A, 266, 106
Barnes, J. E. 1988, ApJ, 331, 699
Fabbiano, G. 1988, ApJ, 330, 672
———. 1989, ARA&A, 27, 87
———. 1995, in X-Ray Binaries, ed. W. H. G. Lewin, J. van Paradijs, & E. P. J. van den Heuvel (Cambridge: Cambridge Univ. Press), 390
Fabbiano, G., Feigelson, E., & Zamorani, G. 1982, ApJ, 256, 397
Fabbiano, G., Schweizer, F., & Mackie, G. 1997, ApJ, 478, 542
Fabbiano, G., & Trinchieri, G. 1983, ApJ, 266, L5
———. 1984, ApJ, 286, 491
Garmire, G. P. 1997, BAAS, 190, 3404
Giacconi, R., et al. 2000, preprint (astro-ph/0007240)
Hasinger, G. 1999, in Cosmological Parameters and the Evolution of the Universe, ed. K. Sato (Dordrecht: Kluwer), 200
Kaaret, P., Prestwich, A. H., Zezas, A., Murray, S. S., Kim, D.-W., Kilgard, R. E., Schlegel, E. M., & Ward, M. J. 2000, MNRAS, 321, L29
King, A., Davies, M. B., Ward, M. J., Fabbiano, G., & Elvis, M. 2001, ApJL, in press
Hummel, E., & van der Hulst, J. M. 1986, A&A, 155, 151
La Parola, V., Peres, G., Fabbiano, G., Kim, D. W., & Bocchino, F. 2001, ApJ, submitted
Makishima, K., et al. 2000, ApJ, 535, 632
Matsumoto, H., Tsuru, T. G., Koyama, K., Awaki, H., Canizares, C. R., Kawai, N., Matsushita, S., & Kawabe, R. 2001, ApJ, 547, L25
Mengel, S., Lehnert, M. D., Thatte, N., Tacconi-Garman, L. E., & Genzel, R. 2000, ApJ, 550, 280
Read, A. M., Ponman, T. J., & Wolstencroft, R. D. 1995, MNRAS, 277, 397
Rubin, V. C., Ford, W. K., & D'Odorico, S. 1970, ApJ, 160, 801
Sansom, A. E., Dotani, T., Okada, K., Yamashita, A., & Fabbiano, G. 1996, MNRAS, 281, 48
Schlegel, E. 1995, Rep. Prog. Phys., 58, 1375
Stanford, S. A., Sargent, A. I., Sanders, D. B., & Scoville, N. Z. 1990, ApJ, 349, 492
Toomre, A., & Toomre, J. 1972, ApJ, 178, 623
Tremaine, S. D., Ostriker, J. P., & Spitzer, L., Jr. 1975, ApJ, 196, 407
Trinchieri, G., & Fabbiano, G. 1990, ApJ, 382, 82
Wang, Q., & Helfand, D. J. 1991, ApJ, 370, 541
Watson, M. G. 1990, in Windows on Galaxies, ed. G. Fabbiano, J. S. Gallagher, & A. Renzini (Dordrecht: Kluwer), 177
Watson, M. G., Stanger, V., & Griffiths, R. E. 1984, ApJ, 286, 144
Weisskopf, M., Tananbaum, H., Van Speybroeck, L., & O'Dell, S. 2000, Proc. SPIE, 4012, 2
Whitmore, B. C., & Schweizer, F. 1995, AJ, 109, 960
Williams, R. M., & Chu, Y.-H. 1995, ApJ, 439, 132
Wilson, C. D., Scoville, N., Madden, S. C., & Charmandaris, V. 2000, ApJ, 542, 120
Zezas, A., Georgantopoulos, I., & Ward, M. 1999, MNRAS, 308, 302
Zezas, A., Fabbiano, G., Ward, M., Prestwich, A., & Murray, S. 2000, BAAS, 197, 9205